

Quantifying secondary particle dose contributions in proton therapy

Hamdi Elsayed

Bachelor of Science Thesis

Quantifying secondary particle dose contributions in proton therapy

BACHELOR OF SCIENCE THESIS

For the degree of Bachelor of Science in Bsc Applied Physics at Delft
University of Technology

Hamdi Elsayed

February 22, 2022

DELFT UNIVERSITY OF TECHNOLOGY
DEPARTMENT OF
DELFT CENTER FOR APPLIED SCIENCES (DCSC)

The undersigned hereby certify that they have read and recommend to the Faculty of Applied Sciences (TNW) for acceptance a thesis entitled

QUANTIFYING SECONDARY PARTICLE DOSE CONTRIBUTIONS IN PROTON THERAPY

by

HAMDI ELSAYED

in partial fulfillment of the requirements for the degree of

BACHELOR OF SCIENCE BSC APPLIED PHYSICS

Dated: February 22, 2022

Supervisor(s):

dr. Z.Perko. T.Burlacu

Reader(s):

dr. Z.Perko

Abstract

In order to create radiotherapy treatment plans for cancer patients, dose calculations need to be done as quickly as possible to get accurate results. However, current dose calculation algorithms take too much time to be deployed effectively. The current in house algorithm of the Medical Physics and Technology Section at the TU Delft, attempts to solve this problem by utilising a deterministic algorithm that has a significant time advantage over Monte Carlo algorithms. However, this comes with the cost of inaccuracy, one of which is that it assumes all dose is deposited locally along the beam path. This is inaccurate as secondary particles created from non-elastic nuclear interactions can deposit their dose far from the beam path due to retaining significant kinetic energy. This thesis attempts to reduce this inaccuracy by mapping and quantifying the secondary particles to assess their contribution in non-local dose deposition. And analysing the relevant particle's energy and angle distributions to gain insight on the development of the particles characteristics with depth. Thereafter the relevant particle's are then utilised as a source to emulate their production in a primary proton beam at different depths to obtain the relevant 3D dose distributions. The analysis concluded that secondary protons are the most relevant secondary particle as they contribute to 88% of the secondary dose and have a significant range to deposit their dose non locally.. By utilising the secondary protons as a source, it was found that the relative error between the integrated depth dose (IDD) of the scored protons and the IDD obtained directly from Monte Carlo simulations is equal to 5.1% in the z-direction and 3.4% in the x and y-direction. The absolute difference was found to be 1.54×10^{-5} Gy which is equal to 0.096% of the total dose and 2.75% of the dose contributed by all secondary particles. The results show that the methodology can produce accurate 3D dose matrices for secondary protons at different depths, which can then be used to improve the accuracy of the in house algorithm by adding the precalculated 3D dose matrices to the algorithm.

Table of Contents

Preface & Acknowledgements	1
1 Introduction	2
1-1 Introduction	2
1-1-1 Radiotherapy	2
1-1-2 Current limitations in treatment planning	4
1-1-3 Research question and Outline of the thesis	4
2 Theoretical framework	6
2-0-1 Proton interactions in matter	6
2-0-2 Monte Carlo simulations	9
2-0-3 The deterministic algorithm	9
3 Experimental setup	11
3-0-1 Selecting the secondary particles	12
3-0-2 Phase Space scoring	13
3-0-3 Dose deposition from Phase Space source	14
4 Results	17
4-0-1 Depth dose distributions	17
4-0-2 Analysing the Phase Space scorers	19
4-0-3 Phase Space source	22
5 Conclusion and recommendations for further research	31
5-0-1 Conclusions	31
5-0-2 Recommendations for further research	32

6 Appendix	34
6-0-1 Configuration of DoseToMedium scorer	34
6-0-2 Configuration of Phase Space scorer	34
6-0-3 Configuration of OriginCount scorer	35
Bibliography	36

List of Figures

1-1	Percentage depth-dose distribution curves of proton beam vs. photon beam. Figure from [1].	3
2-1	Solid line: Bragg peak including nuclear interactions; dashed line: Bragg peak without including nuclear interactions. Figure from [2].	9
2-2	IDD of The deterministic in house algorithm (FE) compared to the probabilistic Monte Carlo algorithm (TOPAS) in a water tank.	10
3-1	The setup used to obtain the depth dose curves. The box is entirely made out of G4_water and is not encased by any other material. Note that the proton beam does not reflect the true path as the beam diverges with depth and has a limited range.	12
3-2	The setup used to score the secondary particles using Phase Space scorers, where the dotted boxes are the Test boxes, which will be assigned a Phase Space scorer. The depth of the Test boxes in the $-\hat{z}$ direction are too small to be shown.	14
3-3	The setup for the Origin Count filters with a focus on the [0,1] cm range. Both the Test boxes as the entire the larger box with measurements (5 cm x 5 cm x 1cm) are assigned a Origin Count filter.	16
4-1	Depth dose distributions (Bragg peak normalized to 100%). The upper figure showcases the primary proton dose, secondary proton dose and the total dose. The lower figure showcases the dose from different secondary particles on a log-scale.	18
4-2	The energy distributions of the secondary protons created at each depth with a spatial resolution of 0.02 cm. The histograms are fitted using a Gaussian Kernel Estimate. The labels contain information about the mean and standard deviations of the energy distributions together with the count of the protons.	20
4-3	Direction cosines of the secondary protons with depth. A negative Direction Cosine Z equates to a forward scattered particle. Note that certain depths were omitted due to lack of relevancy.	21
4-4	Dose distribution of the sum of the scored secondary protons at each depth, visualised by taking a slice at the center of the primary proton beam ($x=2.5\text{cm}$). The white line depicts the spread of the primary proton beam.	23

4-5	The dose deposition due to the protons which were created between 0.48 cm and 0.52 cm and distributed and scaled according to the procedures described in Section 3-0-3. The Grey line depicts the spread of the primary proton beam, while the white line depicts the range on which the particles were distributed.	24
4-6	The dose deposition due to the protons which were created between 3.48 cm and 3.52 cm and distributed and scaled according to the procedures described in Section 3-0-3. The Grey line depicts the spread of the primary proton beam, while the white line depicts the range on which the particles were distributed.	24
4-7	The dose deposition due to the protons which were created between 5.48 cm and 5.52 cm and distributed and scaled according to the procedures described in Section 3-0-3. The Grey line depicts the spread of the primary proton beam, while the white line depicts the range on which the particles were distributed.	25
4-8	The dose deposition due to the protons which were created between 7.48 cm and 7.52 cm and distributed and scaled according to the procedures described in Section 3-0-3. The Grey line depicts the spread of the primary proton beam, while the white line depicts the range on which the particles were distributed.	25
4-9	IDD(z) of the scored secondary protons per depth.	26
4-10	IDD(Y) of the scored secondary protons per depth.	27
4-11	IDD(z) of the Scored secondary protons and the IDD(z) obtained through the simulation setup described in section 3.1	28
4-12	IDD(y) of the Scored secondary protons and the IDD(y) obtained through the simulation setup described in section 3.1	29

List of Tables

4-1	Relative contribution of secondary particles to the total secondary dose deposition in the water box	19
4-2	Ratio of the amount of particles scored by the Origin Count filter in the "larger" box and the Test boxes.	22
4-3	Total dose deposited per depth range and the percentage of the dose that is deposited locally.	28
4-4	IDD(z) and IDD(x/y) and the degree of error calculated using Equation 12. . . .	29

Preface & Acknowledgements

I would like to thank my supervisor dr. Z.Perko for his assistance and advice during the writing of this thesis. Also, I would like to thank T.Burlacu for his help, support and guidance during the research and writing of my thesis. Furthermore, special thanks to Balaj for helping me structure this thesis.

Delft, University of Technology
February 22, 2022

Hamdi Elsayed

Chapter 1

Introduction

1-1 Introduction

Cancer is a disease that is characterized by the uncontrolled growth and spread of cells in the body. This is caused by a mutation in the genes of the cells causing them to ignore signals of apoptosis (self-induced cell death) [3]. Cancer is one of the leading causes of death in the entire world, accounting for 9.5 million cancer-related deaths. The large amount of yearly deaths and the projection that the occurrence of cancer will increase in the coming years due to an aging population, indicates that the development and improvement of treatment methods must continue.

Due to the heterogeneity of cancer cases, no treatment plan is the same. However, most treatment plans consist of treatments such as surgery, chemotherapy, and radiotherapy or a combination of these treatments. In this thesis, the focus will be on the latter treatment, more specifically, a branch of radiotherapy called proton therapy.

1-1-1 Radiotherapy

During conventional photon radiotherapy, the cancerous tumour is irradiated by high energy photons. These photons interact with the atoms of the tissue and deposit their energy with these interactions. During the interaction between the photon and the atoms, the photon can deposit more energy than the ionization threshold causing the atom to get ionized. The ionized electrons can damage the cell's DNA and thus inhibit the cells ability to duplicate. The damage endured by the DNA can slow the growth of the tumour or even cause the tumour to regress. This however, comes with the downside that the photons will also transfer their energy to surrounding healthy tissue causing significant dose deposition in healthy tissue. Due to the percentage depth dose distribution curve of photons which is illustrated in Figure 1-1, the dose deposition to healthy tissue in lower depths is in most cases even relatively higher than the dose deposited to the site of the tumour. To limit the harmful effects of the photon beam to healthy tissue, the tumour is often irradiated from different angles, limiting

the amount of dose deposited at healthy tissue at each angle. However, it has become clear that the minimization over hazardous effects of photon radiotherapy is reaching its physical limits [4].

This development has pushed current research into the development of new methods of radiotherapy, namely proton therapy. The main advantage of proton therapy over conventional radiotherapy using photons is illustrated in Figure 1-1. In contrast to photons, protons deposit relatively low amounts of dose at the entrance of the tissue and relatively higher amounts in a small region called the Bragg peak. The dose deposition after the Bragg peak also decreases rapidly to zero, sparing healthy tissue behind the intended irradiation site. By the addition of multiple energy proton beams, the Bragg peak can be transformed into what is called the Spread-Out Bragg peak, as can be seen in Figure 1-1. This allows the Bragg peak to encompass the entire tumour and thus deliver a high relative dose to the tumour.

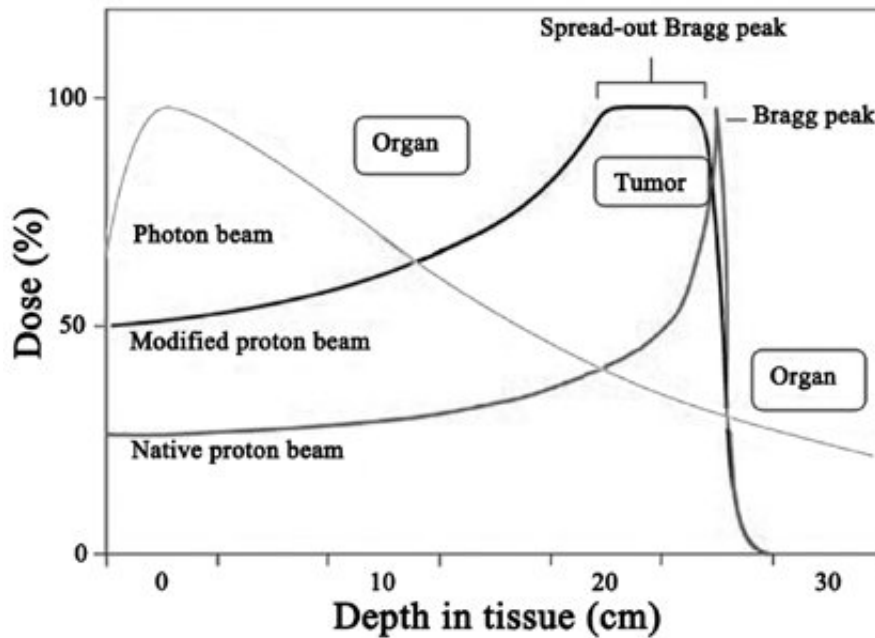


Figure 1-1: Percentage depth-dose distribution curves of proton beam vs. photon beam. Figure from [1].

1-1-2 Current limitations in treatment planning

Radiotherapy requires extensive treatment planning for each unique case to maximize dose deposition on the tumour, while simultaneously minimizing harm to surrounding healthy tissue. The usage of proton therapy requires even greater precision in energy deposition than conventional radiotherapy as protons deposit more of their energy in a smaller range (Bragg Peak) making it more prone to errors.

In proton therapy, the patient geometry is obtained by means of a CT scan, which can then be used to derive the delivery parameters of the required dose. During treatment planning, the CT scans can be a source of uncertainty due to multiple reasons:

- **Uncertainties due to CT conversion:** In proton therapy planning systems, Housefield Unit conversion schemes are implemented to translate Housefield units into relative stopping power. This conversion has an inherent uncertainty [5].
- **Uncertainties due to CT resolution:** In highly heterogeneous geometries, the CT resolution can cause averaging between two different tissues in the calculations leading to inaccurate treatment planning [5].
- **Changes in geometry over time:** The CT scan does not account for changes in body composition over time and is thus outdated when the treatment begins.
- **Movement of tissue during treatment:** During treatment, the patient's bodily functions could alter the geometry of the tumour which makes the treatment plan inaccurate [6].

In light of the third reason, it can be seen that the calculation of a treatment plan should be done in the shortest time possible to limit changes in the geometry over time. However, the most accurate dose calculation algorithm, a Monte Carlo algorithm, is inherently time-consuming as the accuracy is due to the tracking of every proton individually. Currently, the time consumption of Monte Carlo algorithms and the computing power required makes it hard to utilise. This has pushed research into finding more time effective yet relatively accurate approximations.

1-1-3 Research question and Outline of the thesis

In this thesis a deterministic algorithm for calculating dose deposition is discussed. The algorithm's main advantage in comparison to the Monte Carlo method is the time it takes to calculate the dose however, this comes at the cost of the accuracy. One source of inaccuracy is that the algorithm assumes that all dose is deposited locally along the proton beam path. This assumption is not realistic as secondary particles created due to non elastic nuclear interactions still have significant kinetic energy and can thus deposit their dose non locally. This thesis aims to map and quantify the creation of secondary particles in proton therapy beams and accurately calculate the location of their dose deposition. This information will ultimately be used to improve deterministic dose calculation algorithms to provide fast computation times without degraded accuracy.

In chapter 2, a general introduction about proton interactions in a medium will be given, followed by a brief introduction to Monte Carlo algorithms. Lastly, the current deterministic algorithm and its shortcomings will be discussed. In chapter 3, the setups behind the Monte Carlo simulations in TOPAS will be explained. Subsequently, in chapter 4, the results from these simulations together with their significance will be discussed. lastly, in chapter 5, conclusions will be drawn about the results together with a discussion. This is then followed by recommendations for future research. This report is part of a bachelor thesis research of Technology University of Delft at the department of Medical Physics & Technology at the Reactor Institute Delft.

Theoretical framework

In this section, the fundamental theory behind this thesis will be explained. A general introduction to proton interactions in matter will be given, combined with an introduction to the concepts of range and straggling. This is followed by the theory behind TOPAS/Geant4 and Monte Carlo simulations, and lastly, a general introduction to the current deterministic algorithm and its shortcomings will be given.

2-0-1 Proton interactions in matter

The interactions of protons in matter is central to understanding the usability of protons in radiotherapy. In general, protons interact with matter in three distinct ways. Protons lose energy by interacting with the electrons in the matter, transferring energy to the electrons. The protons can also lose energy by deflection through Coulomb interactions with the nucleus. Furthermore, direct collisions with the nucleus will result in energy transfer from the protons to other particles. These processes are called stopping, scattering and nuclear interactions respectively.

Stopping

Stopping is the process of protons interacting with electrons in the material causing energy transfer to the electrons. In most cases, the primary protons transfer enough energy to the electrons to ionize the electrons causing dose depositions by these electrons. In simulations, the dose deposited by the electrons are attributed to the primary protons due to the small range of the ionized electrons. The rate of energy transfer can be quantified by the mass stopping power which is defined in Equation (2-1):

$$\frac{S}{\rho} = -\frac{1}{\rho} \frac{dE}{dx} \quad (2-1)$$

where S is equal to the Stopping Power, E is equal to the energy loss of the proton, and ρ is a correction for the density of the material, which in this thesis will be limited to water and thus

equal to one. From Equation (2-1), it can be seen that the Stopping Power is proportional to the energy loss of the proton in matter. The mass stopping power for protons, specifically in the proton therapy energy range, can be rewritten as [7]:

$$\frac{S}{\rho} = 0.3072 \frac{Z}{A} \frac{1}{\beta^2} \left(\ln \left(\frac{W_m}{I} - \beta^2 \right) \right) \quad (2-2)$$

where $\beta = \frac{v}{c}$ and I is equal to the mean excitation energy of the target material. W_m is defined as:

$$W_m = \frac{2m_e c^2 \beta^2}{1 - \beta^2} \quad (2-3)$$

where m_e is the electron mass and c is the speed of light. From Equation (2-3) it can be seen that the mass stopping power of the proton is inversely proportional to the proton's velocity, which gives rise to the Bragg peak.

Range of particles

The range of a particle is defined as the distance a particle can travel in a specific medium with a particular initial energy. The range can be calculated by integrating the inverse mass stopping power over energy. In this thesis, the range of the particles will be obtained by using data from the National Institute of Standards and Technology [8].

Scattering

Scattering is frequently called Coulomb scattering due to the underlying electrostatic forces. The interaction occurs due to a repellent electrostatic force between the proton and the atom's nucleus. The energy loss due to Coulomb scattering is insignificant compared to energy loss due to stopping or nuclear interactions [9]. However, the contributions to the small angle perturbations due to Coulomb Scattering can significantly alter the primary proton's angle, causing divergence of the primary beam with depth. The sum of all small-angle perturbations will converge to an approximation of a Gaussian due to the Central Limit Theorem. However, this is not precisely the case due to a significant amount of statistical outliers [7].

Nuclear interactions

Nuclear interactions by protons in materials can be separated into three distinct interactions [10]:

- **Elastic Nuclear interactions:** This interaction is characterized by the conservation of total kinetic energy and the absence of change in the state of the incoming particle and the target nucleus. An example of an elastic nuclear interaction is shown in equation (2-4):



- **Inelastic nuclear interactions:** This interaction is defined by absence of conservation of kinetic energy, however, the final nucleus is equal to the target nucleus. An example of a inelastic nuclear interaction is shown in equation (2-5):



Where the ${}^{16}\text{O}^*$ denotes an excited state of the oxygen atom.

- **Nonelastic nuclear interactions:** This interaction is characterized by the absence of kinetic energy conservation combined with a change in the target nucleus. An example of a nonelastic nuclear interaction is shown in equation (2-6):



The dose from secondaries created by nonelastic nuclear interactions is small compared to the dose from the primary protons; however they should be included in dose calculations during treatment planning [9], which is currently done in the algorithm discussed in chapter 2-0-3. This is because secondary particles can deposit their dose far from the primary proton beam path causing damage to surrounding tissue. This is even more concerning due to the high ionization density of some secondaries [7].

In this thesis, only the most probable secondary particles will be investigated, namely secondary Protons, Neutrons, Deuterons, Tritons, Alphas and Helium-3 [11].

Straggling

Straggling is the statistical variation around the mean of the energy loss of a proton in a material. The consequence of straggling is the increased spread in the energy of the primary proton beam. Since the energy of a particle and its range are related, the energy straggling also results in range straggling [12]. In Monte Carlo algorithms straggling is accounted for due to the probabilistic nature of the algorithm. However, it needs to be accounted for in deterministic algorithms like the in house algorithm.

The Bragg peak and nuclear interactions

The Bragg peak is a characteristic of the depth dose distribution created by a proton beam in matter. It is primarily caused by the inverse relation between the mass stopping power and the proton's velocity. Meaning that the proton transfers more energy per unit length to target particle at lower energies. The position of the Bragg peak is thus a function of the primary proton energy.

Non elastic nuclear interactions significantly impact the shape of the Bragg Peak as these nuclear interactions create secondary particles that can deposit a significant amount of energy non-locally. This causes a lower Bragg Peak but a higher relative dose deposition at the entrance region. This effect can be seen in Figure 2-1.

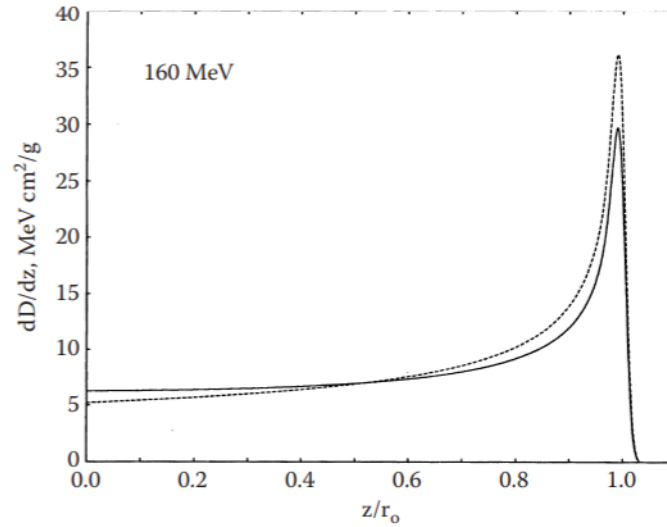


Figure 2-1: Solid line: Bragg peak including nuclear interactions; dashed line: Bragg peak without including nuclear interactions. Figure from [2].

2-0-2 Monte Carlo simulations

In this thesis, simulations based on Monte Carlo techniques will be used to simulate the physics of proton transport on a step by step basis. The simulation tool that will be used during this thesis is called TOPAS, which is an extension of the Geant4 Simulation Toolkit [13]. Monte Carlo simulations sample from pseudo-random numbers, which are then used to sample from empirically obtained probability density functions to simulate the physics of the proton interactions for every step length. The distributions are based on the cross-sections, which is a measure of the probability that a certain process will occur. Thus, Monte Carlo simulations get more accurate whenever a shorter step length is used as this more closely approximates the Linear Boltzmann equations being solved. However, this requires more computing power increasing the simulation time.

In order to understand the results of the Monte Carlo simulations, some definitions need to be made clear.

1. **Secondaries:** A secondary is defined as anything that is not primary.
2. **Original Histories:** Original histories are the entire trajectories of the primary particles (in this thesis, protons) and their secondary particles.

2-0-3 The deterministic algorithm

The deterministic algorithm solves the Linear Boltzmann Equation (LBE) to model the movement of protons through the medium. The LBE is defined as:

$$\hat{\Omega} \cdot \nabla \phi(\vec{x}, E, \hat{\Omega}) + \sigma_t \phi(\vec{x}, E, \hat{\Omega}) = \int_{4\pi} \int_0^\infty dE' \sigma_s(\vec{x}, E' \rightarrow E, \hat{\Omega}' \rightarrow \hat{\Omega}) \phi(\vec{x}, E, \hat{\Omega}) d\hat{\Omega} \quad (2-7)$$

where $\hat{\Omega}$ is the direction of the particle of interest, E is the energy, \vec{x} is equal to the position, and ϕ is equal to the flux. The quantities σ_t and σ_s are the total cross-section and the total scatter cross-section, respectively. The derivation of the LBE can be found in the works of Dudderstadt and Hamilton [14]. The first term on the left hand side of the equation describes the net flow of particles from a volume element about \vec{x} . The second part of the left-hand side of the equation describes the total loss of particles due to collisions. The probability of these collisions are governed by the total macroscopic cross-section σ_t . The right hand side of the equation represents the scatter of particles with initial energy E' , and direction Ω' and subsequently gain energy E and direction $\hat{\Omega}$ after scattering [15].

By using several assumptions, the LBE is transformed into two partial differential equations, which are the Fokker-Planck equation and the Fermi-Eyges equation [16]. These partial differential equations can then be solved semi-numerically to obtain the movement of the proton through the medium.

The current in house algorithm has the advantage that it is fast in comparison to Monte Carlo dose calculations. However, this comes at a cost of accuracy. One of these inaccuracies is that the model does not take in to account the trajectories of secondary particles and thus assumes that all the dose from the secondary particles is deposited locally. This is incorrect, as secondary particles can deposit their dose far deeper in to the tissue. This causes the dose to be overestimated in the entrance region and thus underestimated in more considerable depths around the Bragg Peak as can be seen in Figure 2-2.

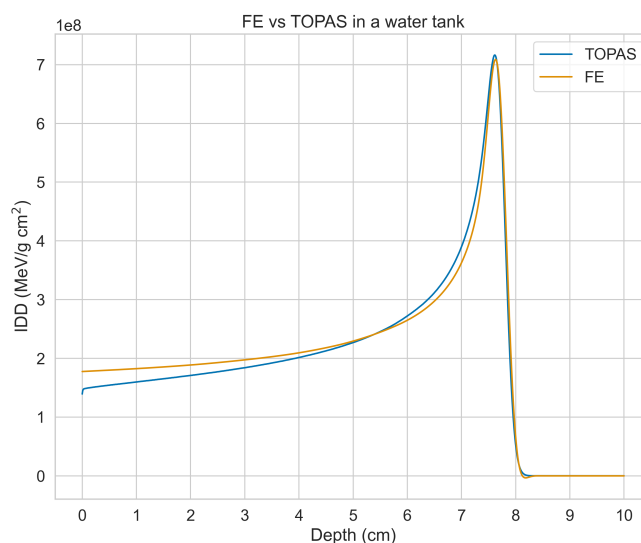


Figure 2-2: IDD of The deterministic in house algorithm (FE) compared to the probabilistic Monte Carlo algorithm (TOPAS) in a water tank.

Chapter 3

Experimental setup

In order to identify which secondary particles contribute significantly to non-local dose deposition, a selection must be made based on the secondary particles with the highest total dose deposition and range. This will be done in Sections 3-0-1 and 3-0-2. In Section 3-0-2, the methodology for extracting the energy and angle distributions via a Phase Space scorer is illustrated. In Section 3-0-3, the dose deposition from the secondary particles will be derived by using the scored secondary particles as a source.

In this Section, all simulations have been done using the TOPAS Geant4_Modular option with the recommended modules for proton therapy applications. The physics lists which are included and their properties are shown below:

- **g4em-standard_opt4**: Governs the electromagnetic physics such as multiple Coulomb scattering.
- **g4h-phy_QGSP_BIC_HP**: Governs elastic, inelastic and capture processes of hadrons.
- **g4decay**: Handles the decay of long-lived hadrons and leptons.
- **g4ion-binarycascade**: Models interactions of nucleons, pions, and light ions with nuclei [17].
- **g4h-elastic_HP**: Governs hadronic physics for low energy
- **g4stopping**: Governs the nuclear capture at rest of negatively charged particles.

For more information on the used physics lists the Geant4 physics list guide can be consulted [18].

The simulations have been completed using a range cut for all particles at 0.05 mm, which means that no particle with a range smaller than 0.05 mm was created or tracked. The range cut was put in place to reduce simulation times.

3-0-1 Selecting the secondary particles

To assess which secondary particles are of interest in this thesis, the particles will be judged on two main characteristics:

1. **Dose deposition of the particle:** If the particle of interest does not contribute significantly to the secondary dose, it can be disregarded to simplify the experiments and to reduce the complexity of further analysis without significant loss of accuracy.
2. **Particle range in water:** If the particle of interest does not have sufficient range, then the current assumption in the in house algorithm that the dose is deposited locally is a sufficient approximation. Disregarding these particles will thus not result in a significant decrease of accuracy in the current in house algorithm.

Obtaining the depth dose curves

In an effort to eliminate secondary particles which do not contribute significantly to the total dose deposition a depth dose curve was made. In order to be able to set up a simulation, a geometry had to be created first. The geometry in the case of obtaining the depth dose distributions is a simple water box with the dimensions of 10 cm x 5 cm x 5 cm (length x width x height). Where the length of the box is distributed along the $-\hat{z}$ direction. The setup is shown below in Figure 3.

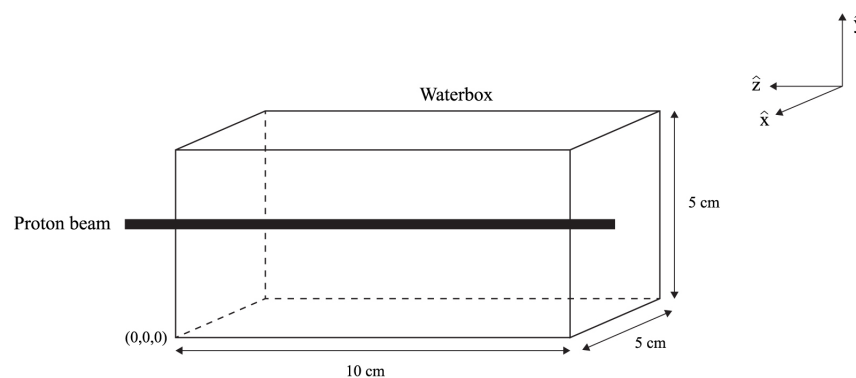


Figure 3-1: The setup used to obtain the depth dose curves. The box is entirely made out of G4_water and is not encased by any other material. Note that the proton beam does not reflect the true path as the beam diverges with depth and has a limited range.

The origin of the coordinate system will be chosen at the left-hand side of the box, as shown in Figure 3. The box is made exclusively of G4_water, which has a density of $1g/cm^3$ and a mean excitation energy of 78.0 eV. The proton beam is defined as a Gaussian pencil-beam with energy $\mu = 100$ MeV and $\sigma = 0.757504$ MeV and a positional spread in x and y of 0.3 cm respectively. The center of the beam originates from the position $(x,y,z) = (2.5,2.5,0)$ and traverses in the $-\hat{z}$ direction. The beam starts with 10 million original histories.

To obtain the depth dose distributions, a DoseToMedium scorer is used to divide the water box into a 3D voxel grid and measure the deposited dose per voxel by using the sum of energy deposits divided by the mass of the voxel. In the case of this simulation, the water box is divided in a 256 x 256 x 512 voxel grid. This means that the deposited dose per voxel is defined as:

$$Dose = \frac{\sum_i E_i}{\rho V} = \frac{\sum_i E_i}{\rho \frac{5cm}{256} \frac{5cm}{256} \frac{10cm}{512}} \quad (3-1)$$

where the dose is in Gray, $\sum_i E_i$ is equal to the total energy deposition in a voxel and ρ , V are the density of the medium and the volume of the voxel respectively. The scorers are then filtered on a particle basis and thus the 3D dose matrix of all scored particles can be obtained separately. For the entire DoseToMedium scorer configuration, the Appendix can be consulted.

Range of particles

The particles with sufficient contribution to the total dose will then be assessed using known literature to obtain information about the range of the particles in water. If the range on average does not allow the particle to travel outside total width of the primary proton beam, then the current assumption in the in house algorithm that the dose is deposited locally is a sufficient approximation. Thus, the particles can be disregarded without significant loss of accuracy.

3-0-2 Phase Space scoring

In order to analyse the quantitative properties of secondary particles created in the Water Box, a Phase Space scorer was used. A Phase Space scorer is a scorer that stores data of a particle crossing a certain surface. The same setup as in Figure 3-1 was used, only this time the water box contained smaller boxes (Test boxes) at $\frac{(2i-1)}{2}$ cm for $i=1,2..10$ which will have the dimensions 1.5 cm x 1.5 cm x 0.04 cm. The lateral dimensions have been chosen to encompass the entire width of the beam during the entire range as the beam spreads out with depth and to include secondary particles which are created further from the primary proton beam path by other secondaries. These can, for example, occur due to the (n,pn) reaction in which a secondary neutron can liberate a secondary proton outside the entire beamwidth. The length of the box in the $-\hat{z}$ direction is made to be very small (0.04 cm) to preserve spatial resolution and to capture particles with a very small range created in the box as the particles are only scored on the surfaces of the box. For the entire Phase Space scorer configuration, the Appendix can be consulted.

The setup can be seen in Figure 3-2:

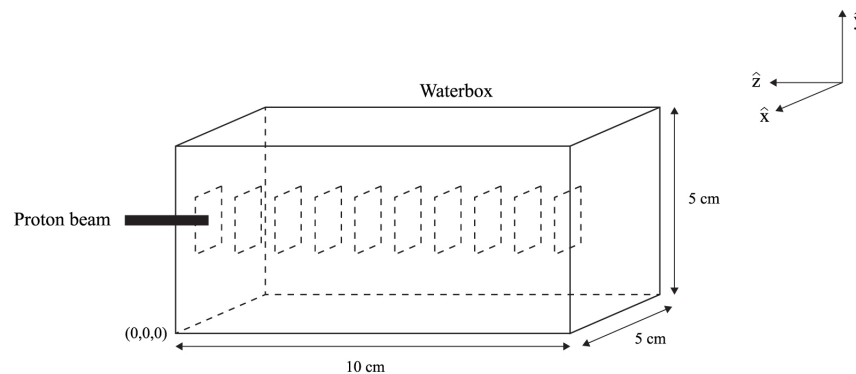


Figure 3-2: The setup used to score the secondary particles using Phase Space scorers, where the dotted boxes are the Test boxes, which will be assigned a Phase Space scorer. The depth of the Test boxes in the $-\hat{z}$ direction are too small to be shown.

The data that is scored and utilised in this thesis are:

- **The position of the particle:** The position of the particle in x, y and z is recorded.
- **The Energy:** The energy of the particle in MeV is stored.
- **Particle type:** The type of particle e.g. proton or neutron.
- **The Direction cosine:** The direction cosines with respect to the axes are recorded. The direction cosines are defined as:

$$\text{Direction cosine } i = \frac{\mathbf{v} \cdot \hat{e}_i}{\|\mathbf{v}\|} \quad (3-2)$$

where $i \in \{x,y,z\}$, \hat{e}_i is a unit vector and $\mathbf{v} = v_x\hat{e}_x + v_y\hat{e}_y + v_z\hat{e}_z$.

Each box was assigned a Phase Space scorer and was set only to score the particles created within the box. To obtain sufficient data of the particles, enough particles had to be created within the boxes. This was done by setting the amount of original histories to 200 million in order to increase the probability of a particle being created within the Test boxes. The data from the Phase Space scorers were then analysed using Python, which gave insight into the particles' energy and angle distribution. The analyzed data was then used to obtain the range of the particles to select which particles will be used in further experiments and to bring insight into the development of the characteristics over depth.

3-0-3 Dose deposition from Phase Space source

After analysing the particles in Python, the scored particles could then be used as a particle source in TOPAS. The Phase Space scorer is essentially a snapshot in time of the particles, thus allowing the particles to restart from a specific position with the same position, energy

and angle distribution as they were scored. The setup for the simulation is the same as in section 3.1, however, the source will not be a pencil beam of primary protons but the particles scored using the Phase Space scorer. To obtain the 3D deposition matrix of a Phase Space source, the following is done:

1. For each Phase Space scorer separately, the particles were randomly distributed along the original proton beam path. For example, the scorer at 0.5 cm had the particles distributed from $z=0$ cm to $z=1$ cm and distributed normally over x and y with a mean of 0 cm and a standard deviation of 0.3 cm to replicate the primary proton beam.
2. The Phase Space source was then filtered on a specific particle and used as a source.
3. The scored particles distributed along the beam path will then start from the assigned position with the scored energy and angle distributions.
4. The 3D dose deposition matrix is then obtained for the source using the DoseToMedium scorer, which is explained in Section 3-0-1.

For this method to be valid, characteristics of the secondary particles need to be constant along the distributed path. This is due to the particles only being measured at the surfaces of the Phase Space scorers, which are positioned at the mean of the range with a spatial resolution of ± 0.02 cm. In the analysis of Section 3-0-2, this was shown to be a valid assumption for most of the water box. In chapters 4 and 5, the results will be discussed in further detail.

Scaling using Origin Count

Using the method described in Section 3-0-3 the only particles that deposit dose are the particles scored from the Phase Space scorer. However, the particle source was distributed along a larger range, so the particles had to be scaled accordingly. The scaling was done using the Origin Count filter, which is a filter in TOPAS that counts the reactions products in a certain volume. This is done by analysing the amount of steps the particle has taken within a specific volume, if the amount of steps is equal to one, then the particle must have been created in the given volume. This is using the assumption that the step size is smaller than the volume, which is assumed to be valid as the Monte Carlo process adapts its step size to the geometry [13].

The origin count filters were then assigned to the Test Boxes from Section 3-0-2 and to new boxes that encompass the entire volume of the water box with a depth equal to the range over which the particles were distributed. The setup for the origin count filter for scaling of the particles scored at $0.5 \text{ cm} \pm 0.02 \text{ cm}$ can be seen in Figure 3-3 .

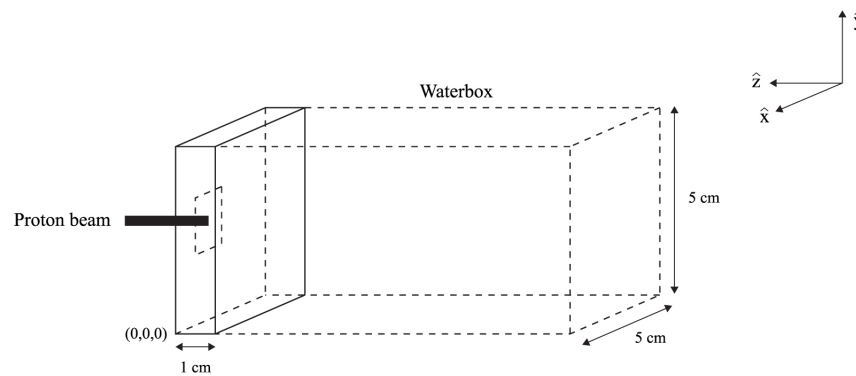


Figure 3-3: The setup for the Origin Count filters with a focus on the $[0,1]$ cm range. Both the Test boxes as the entire the larger box with measurements (5 cm \times 5 cm \times 1cm) are assigned a Origin Count filter.

The number of particles created in the larger box was then divided by the number of particles created in the Test Box. This ratio is called the multiplication factor. This was then repeated for each range. The multiplication factor is essentially reusing the same particle multiple times to obtain the dose that would have been deposited if all secondary particles in the range were scored and used as a source. The obtained multiplication factors were then used to scale the particles' dose deposition, which was found in Section 3-0-3.

Chapter 4

Results

4-0-1 Depth dose distributions

By using the simulation setup described in section 3-0-1, the 3D dose distributions of the selected particles were obtained. In order to showcase the 3D dose distributions efficiently, the 3D dose matrix is converted into a 1D Dose matrix, the so-called integrated depth dose (IDD).

$$IDD(z) = \sum_{x=1}^m \sum_{y=1}^n D_{xyz} \Delta x \Delta y \quad (4-1)$$

Where D_{xyz} is equal to the 3D dose matrix, m and n are equal to the length of the matrix in x and y respectively and Δx , Δy are equal to the width of the voxels in x and y respectively. The integrated depth dose can be plotted in the $-\hat{z}$ direction. In order to quantify the relative contribution of each particle to the total dose effectively, the Bragg peak is normalized to 100%. The results are shown in Figure 4-1.

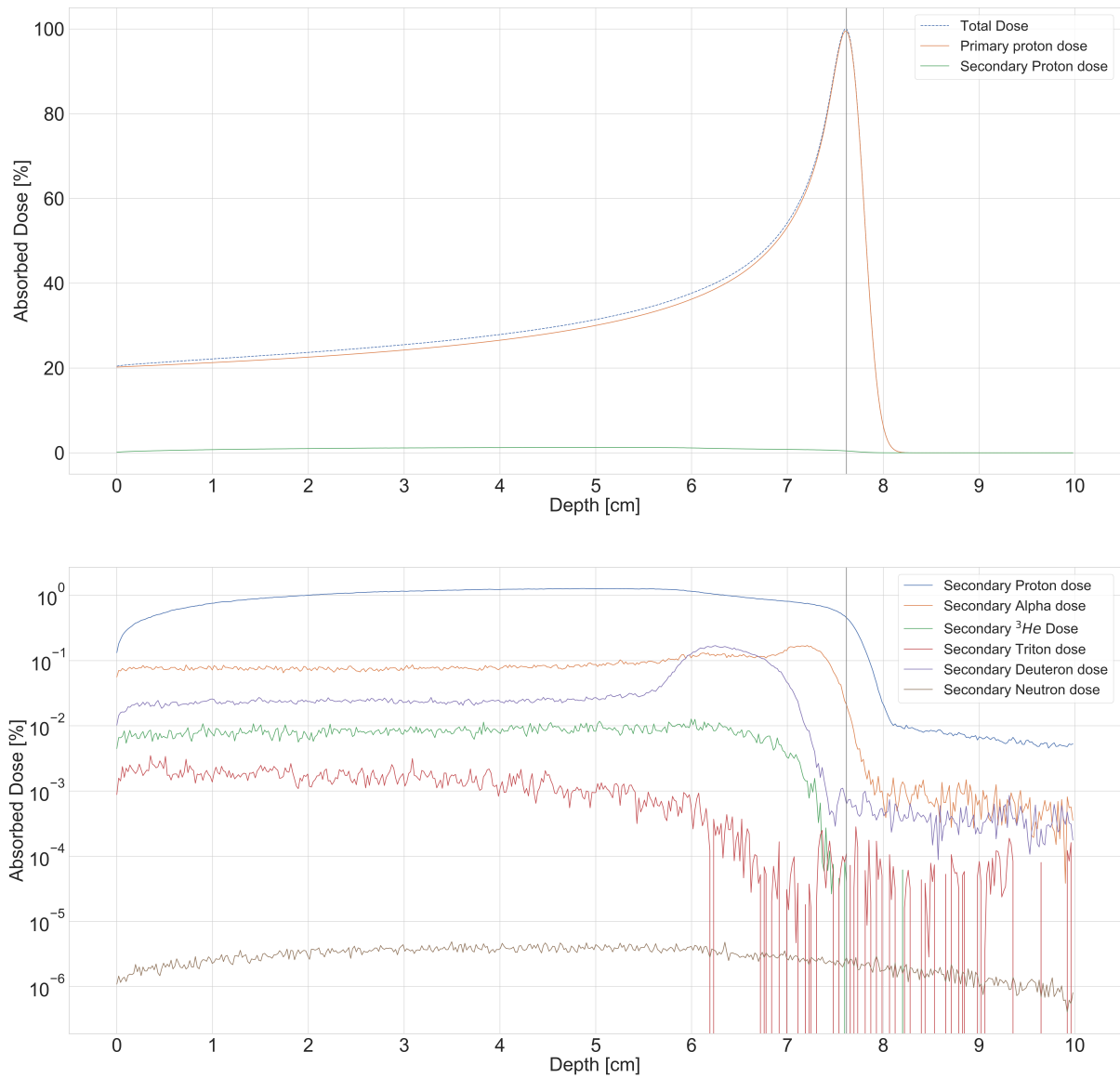


Figure 4-1: Depth dose distributions (Bragg peak normalized to 100%). The upper figure showcases the primary proton dose, secondary proton dose and the total dose. The lower figure showcases the dose from different secondary particles on a log-scale.

The findings show that the dose contributions due to secondary particles only totals around 3.2% of the total dose contributions, which is equal to 0.016 [Gy]. These values are obtained by summing up all dose from the voxels and multiplying them by their respective mass. The 3.2% of the total dose contribution can then be further divided between the particles as can be seen in Table 4-1.

Table 4-1: Relative contribution of secondary particles to the total secondary dose deposition in the water box

Secondary particle	Relative contribution	Absolute contribution [Gy]
Proton	88%	4.51×10^{-4}
Alpha	7.8%	3.99×10^{-5}
Deuteron	3.4%	1.74×10^{-5}
Triton	0.1%	5.12×10^{-5}
Neutron	0.0003%	1.54×10^{-9}
Helium-3	0.67%	3.43×10^{-7}

The results from the simulation are in accordance with the results from the literature [11]. From these results, it can be concluded that only taking into account primary protons should be sufficient. However, Alpha particles seem to contribute significant dose as well and thus have to be included in the simulations.

Selection based on range

In section 4-0-1, it was concluded that secondary protons together with secondary alpha particles account for approximately 96% of the dose deposited by secondary particles. In order to conclude which particle to further analyse in later experiments, it is of importance to know if the particles will deposit their dose non locally. This is done by analysing the particles range for the energy spectrum that occurs during collisions with primary protons.

Using the possible energy domain of secondary alpha particles in the context of this experiment, which are obtained through the Phase Space scorers, it can be derived that the range of the secondary alpha particles will always be lower than 0.257 cm. Which is in contrast with the range of secondary protons, which can reach up to a range of 5.21 cm [8]. The range of alpha particles is thus smaller than the total width of the primary proton beam, which suggests that most secondary alpha particles will deposit their dose locally. This is in line with expectations as alpha particles have an electrostatic charge of +2, which causes them to be highly ionizing, resulting in rapid energy loss. Which is in contrast with secondary protons who have the potential to deposit their dose beyond the total width of the primary proton beam. For this reason, in the further analysis, only the secondary protons will be accounted for.

4-0-2 Analysing the Phase Space scorers

After the selection process, the secondary protons were scored using a Phase Space scorer which obtains information about the energy and angle distributions of the secondary protons.

Energy distributions of secondary protons

From the Phase Space scorers the following energy distributions for the secondary protons were obtained, which are illustrated in Figure 4-2.

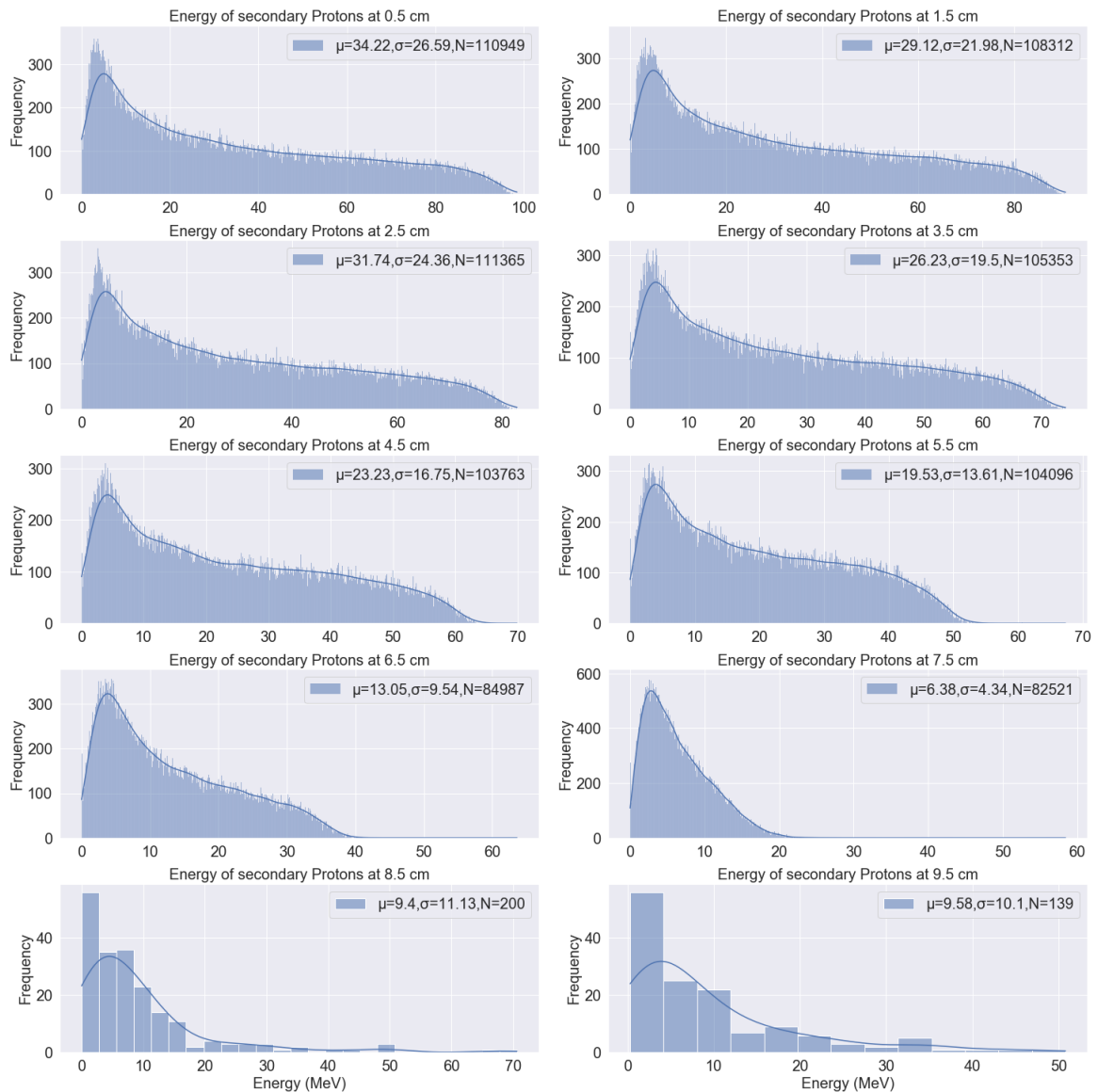


Figure 4-2: The energy distributions of the secondary protons created at each depth with a spatial resolution of 0.02 cm. The histograms are fitted using a Gaussian Kernel Estimate. The labels contain information about the mean and standard deviations of the energy distributions together with the count of the protons.

The energy distributions of the secondary protons show an inverse relationship between mean energy and depth. The literature supports this as the primary protons also lose energy while

traversing through the water tank through other means such as inelastic interactions and scattering [7]. From Figure 4-2 it can also be seen that up until 7.5 cm the amount of secondary protons are significantly higher than the amount thereafter. This is due to the location of the Bragg peak of the primary protons which is located at 7.61 cm as can be seen in Figure 4-1. After the Bragg Peak, the energies of the primary protons drop quickly to close to zero and thus cannot create new secondary protons in more considerable depths. The secondary protons after the Bragg Peak are most likely the result of liberation through the (n,pn) reaction as secondary neutrons have a large range due to the neutral charge.

Angle distributions of secondary protons

From the Phase Space scorers the following angle distributions for the secondary protons were obtained.

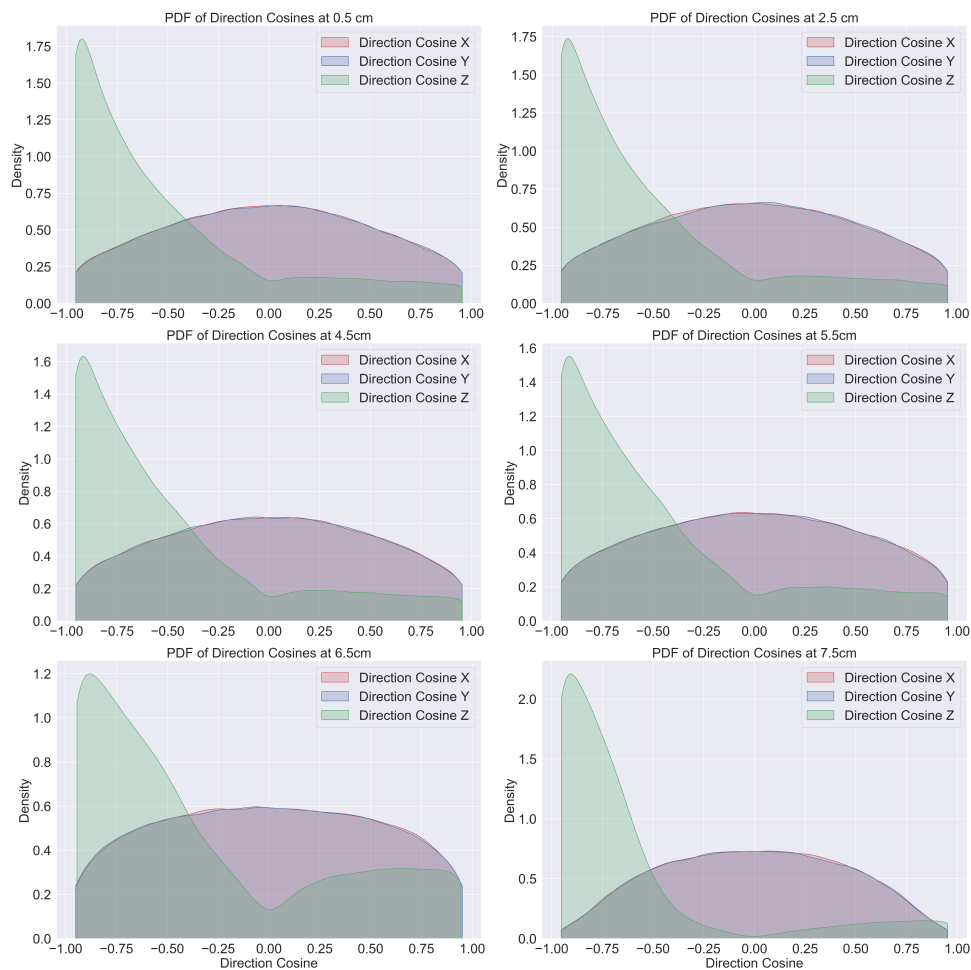


Figure 4-3: Direction cosines of the secondary protons with depth. A negative Direction Cosine Z equates to a forward scattered particle. Note that certain depths were omitted due to lack of relevancy.

Figure 4-3 shows that there is a consistent symmetry for the Direction Cosine in X and Y, which is in line with expectation as the primary proton beam is a Gaussian which has an equal spread in both the \hat{x} and \hat{y} direction. The higher frequency of the particles traversing in the $-\hat{z}$ is in line with expectations, as to conserve total momentum, the vast majority of secondary protons should traverse in the same direction as the primary proton beam. The average percentage of forward scattered secondary protons is equal to 84%, which is approximately constant with depth except at 6.5 and 7.5 cm, where the percentage of forward scattered protons is equal to 72% and 89% respectively. The lower amount of forward scattered protons at 6.5 cm could be explained by the high reaction probability of (p,2p'n) reaction, which results in more backward scattered secondary protons. While at 7.5 cm, the protons are mainly created by (p,p') and (p,2p') reactions, resulting in more forward scattered protons. While in the rest of the beam path, the reactions are a combination of all possible reactions [11].

4-0-3 Phase Space source

The scored secondary protons were then used as sources as described in Section 3-0-3. In order to scale to the expected amount of particles, the Origin Count filter was used as described in section 3-0-3. The results from the scaling are shown in Table 4-2:

Table 4-2: Ratio of the amount of particles scored by the Origin Count filter in the "larger" box and the Test boxes.

Depth range	Ratio
[0-1] cm	27.1
[1-2] cm	27.5
[2-3] cm	28.7
[3-4] cm	28.8
[4-5] cm	29.5
[5-6] cm	29.3
[6-7] cm	30.5
[7-8] cm	22.9
[8-9] cm	43.7
[9-10] cm	22

From Table 4-2, it can be seen that most ratios have been found in the range of 25-30. This is in line with expectations as the volume of the Test Box, which has a scorer assigned, has a lateral dimension equal to 1.5 cm. Meaning that it encompasses the entire lateral dimension of the primary proton beam. However, the scorer has 1/25 the depth of the larger box, which explains the ratios of 25-30. If the Ratio is significantly larger or smaller than 25, then that is an indication that the position of the scorer is not a good indication of the amount of created particles in the entire range. This is for example the case in the [7,8] cm and [8,9] cm range, which is explained by the rapid changes in amount of secondary protons being created due to the Bragg Peak occurring in that region.

Dose deposition due to Phase Space Source

Using the methodology described in section 3-0-3, the 3D dose matrix from the scored secondary protons were obtained at each depth. In order to visualise the dose deposition from the secondary protons, a slice is taken at the center of the box at $x=2.5$. This location corresponds with the center of the primary proton beam and is thus the slice where the highest occurrence of secondary protons is expected due to the Gaussian shape of the primary proton beam. **It is important to note that from now on the \hat{z} direction is used as the depth of the Water Tank.** The shape of the total dose deposition is shown in Figure 4-4.

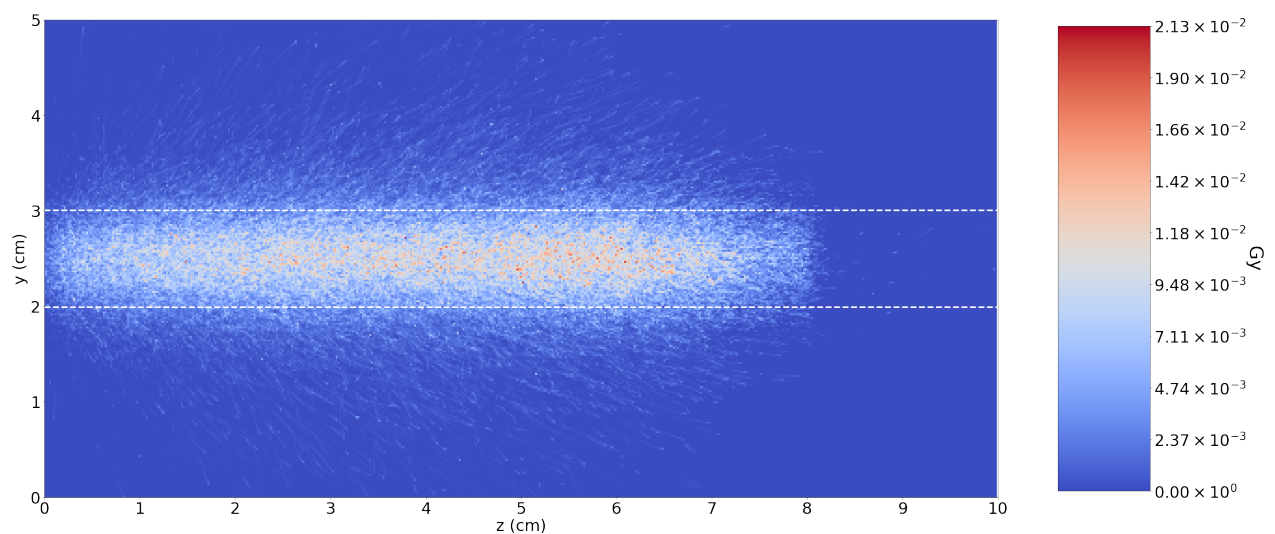


Figure 4-4: Dose distribution of the sum of the scored secondary protons at each depth, visualised by taking a slice at the center of the primary proton beam ($x=2.5\text{cm}$). The white line depicts the spread of the primary proton beam.

Figure 4-4 shows that there is significant dose deposition beyond the spread of the primary protons, confirming that the current assumption that the dose deposition of the secondary protons is deposited locally is incorrect. Figure 4-4 also follows the expected dose deposition distribution with depth [7]. The dose deposition distribution shows a lower dose deposition in the entrance followed by a gradual increase in dose deposition, which eventually reaches its peak just before the Bragg Peak. It can also be seen that the dose deposition has a distinct cut off at the 8 cm mark, which suggests that the discrete measurements do not represent the theoretical result correctly around the Bragg Peak as was also indicated by the results from Table 4-2.

In order to understand the evolution of the dose deposition from secondary protons with depth, the dose deposition at different depths will be visualised in Figure 4-5, 4-6, 4-7 and 4-8 using the same methodology as before.

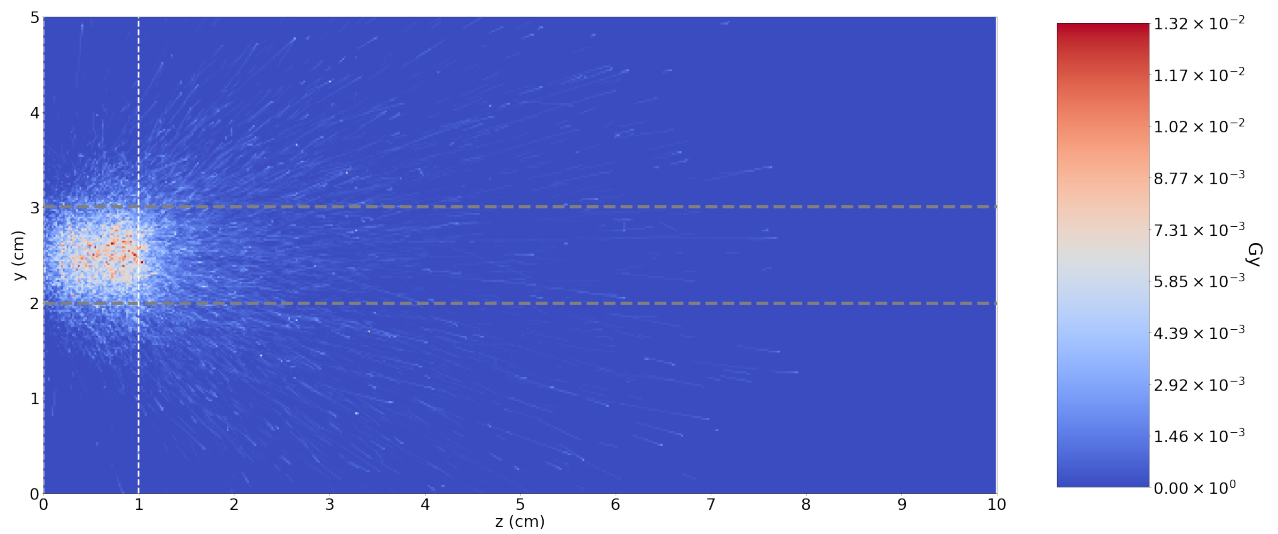


Figure 4-5: The dose deposition due to the protons which were created between 0.48 cm and 0.52 cm and distributed and scaled according to the procedures described in Section 3-0-3. The Grey line depicts the spread of the primary proton beam, while the white line depicts the range on which the particles were distributed.

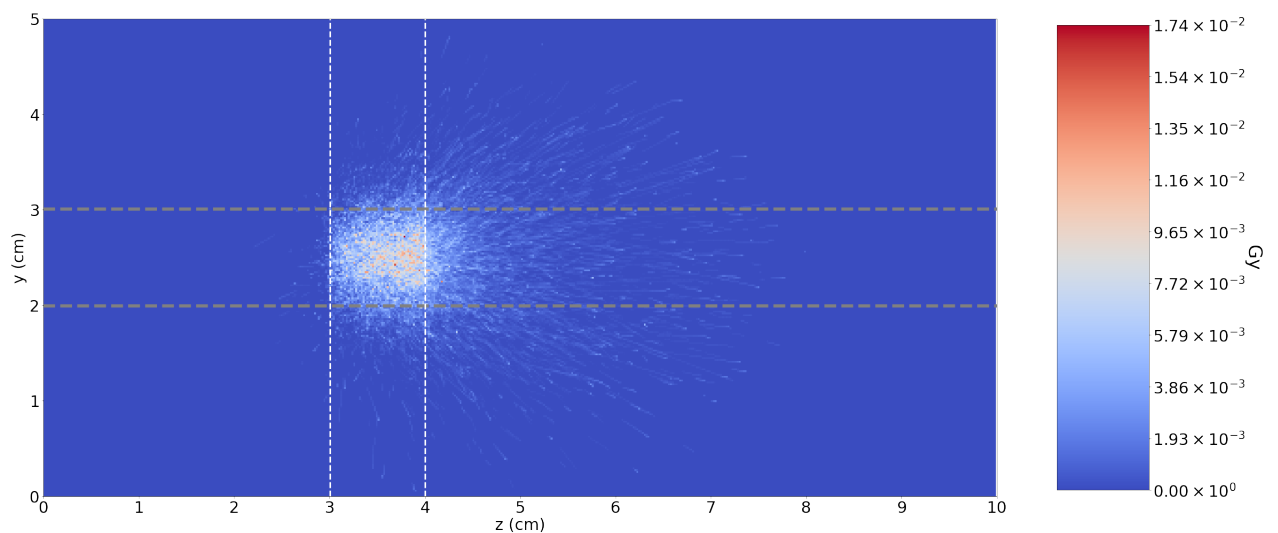


Figure 4-6: The dose deposition due to the protons which were created between 3.48 cm and 3.52 cm and distributed and scaled according to the procedures described in Section 3-0-3. The Grey line depicts the spread of the primary proton beam, while the white line depicts the range on which the particles were distributed.

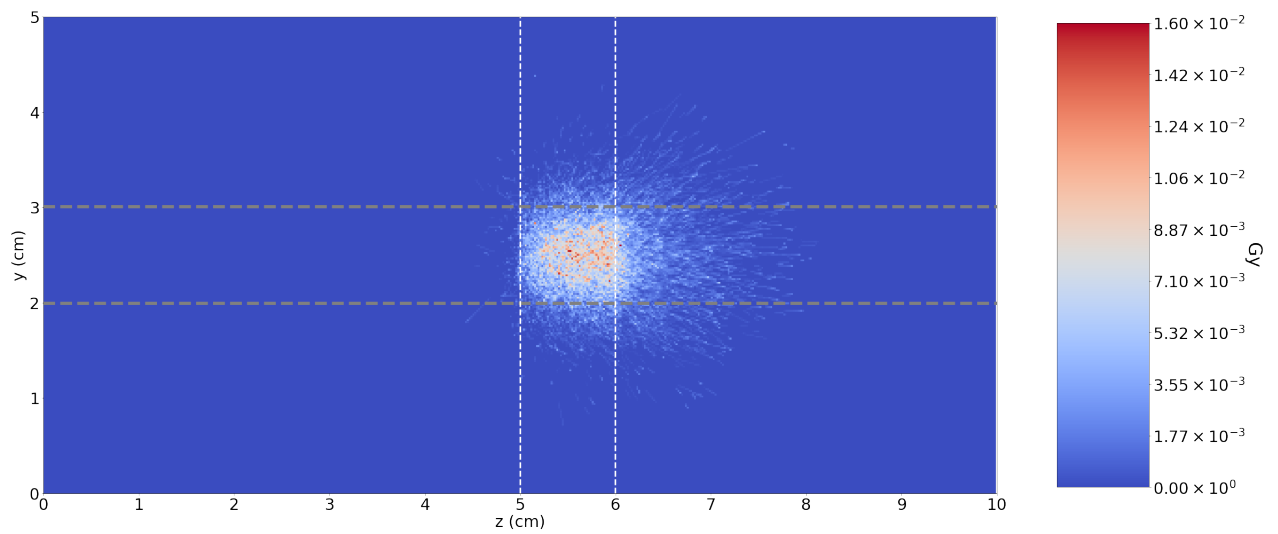


Figure 4-7: The dose deposition due to the protons which were created between 5.48 cm and 5.52 cm and distributed and scaled according to the procedures described in Section 3-0-3. The Grey line depicts the spread of the primary proton beam, while the white line depicts the range on which the particles were distributed.

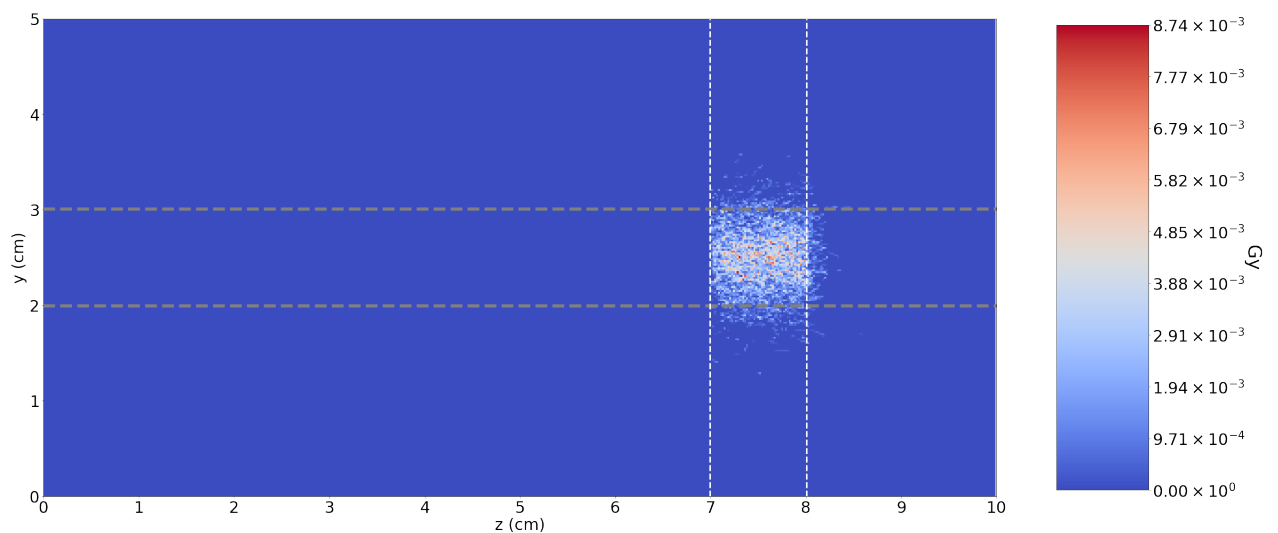


Figure 4-8: The dose deposition due to the protons which were created between 7.48 cm and 7.52 cm and distributed and scaled according to the procedures described in Section 3-0-3. The Grey line depicts the spread of the primary proton beam, while the white line depicts the range on which the particles were distributed.

Figures 4-5, 4-6, 4-7 and 4-8 illustrate that the dose deposition from the secondary protons becomes more local with depth. This is in line with expectations as the energy of the secondary protons decrease with depth as can be seen in Figure 8, which in turn decreases the range of the secondary protons.

In order to further quantify the dose distributions due to the scored secondary protons, the $IDD(z)$ is obtained using Equation (10), however in order to quantify the spread in the lateral direction, the $IDD(y)$ is derived, which is defined as:

$$IDD(y) = \sum_{x=1}^m \sum_{z=1}^n D_{xyz} \Delta x \Delta z \quad (4-2)$$

The $IDD(x)$ is omitted due to symmetry in the angular distributions of the secondary protons, as can be seen in Figure 4-3. This suggests that $IDD(x)$ is approximately equal to $IDD(y)$. The $IDD(z)$ and the $IDD(y)$ are shown below. Due to the negligible dose, the measurements after the Bragg peak are omitted.

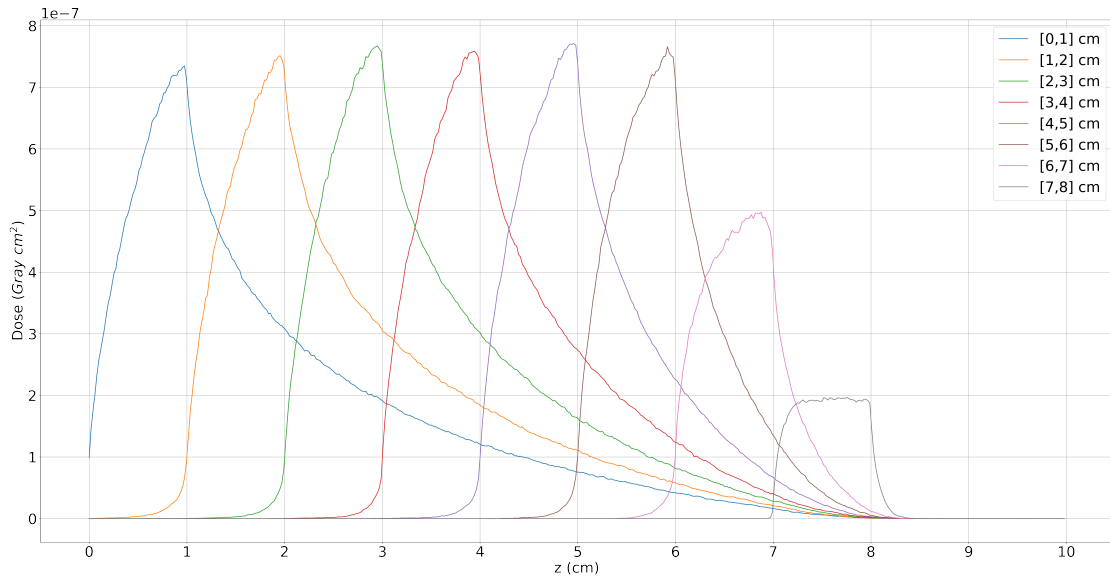


Figure 4-9: $IDD(z)$ of the scored secondary protons per depth.

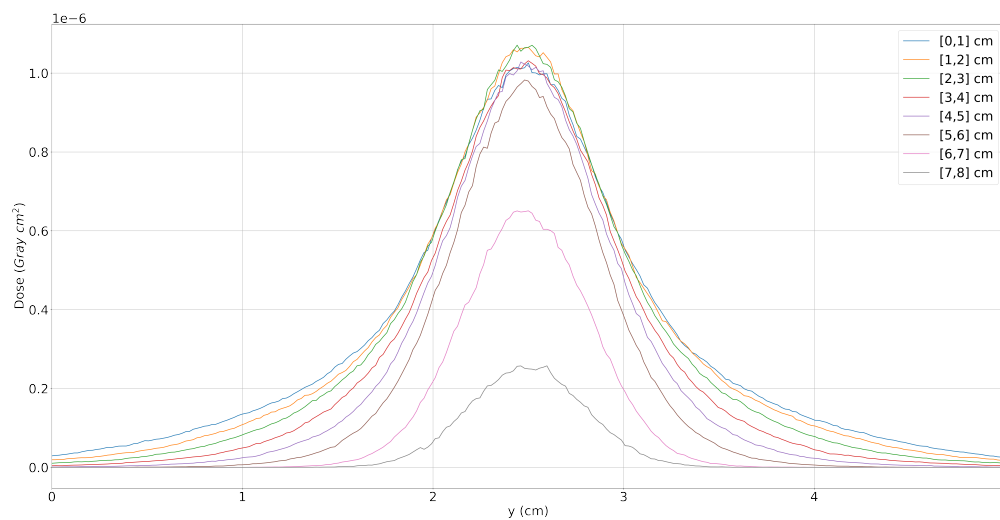


Figure 4-10: IDD(Y) of the scored secondary protons per depth.

Figure 4-10 and 4-9 show that in both the dose deposition the y-direction (and thus also the x-direction) and the z-direction local dose deposition increases with depth. The left tail of IDD(z) in Figure 4-10 in the [0,1] cm range explains the low energy deposition in the entrance region as the dose is abruptly cut off due to the particles backscattering out of the Water Tank. This, combined with the fact that the particles deposit their dose non locally provides an explanation for the low energy deposition of secondary protons in the entrance region. In order to further quantify the difference between the definition of local and non-local dose deposition, the concept of local deposition is defined as:

1. The dose is deposited in the total primary proton width which is from 2 to 3 cm.
2. The dose is deposited within the range of the secondary proton e.g. a secondary proton which is started from 2.3 cm should deposit its dose between 2 and 3 cm.

Using this definition Table 4-3 is derived.

Table 4-3: Total dose deposited per depth range and the percentage of the dose that is deposited locally.

Depth	Total dose [Gy]	% of dose deposited locally
[0,1] cm	7.90×10^{-5}	21.6
[1,2] cm	7.67×10^{-5}	23.4
[2,3] cm	7.25×10^{-5}	25.8
[3,4] cm	6.45×10^{-5}	28.9
[4,5] cm	5.78×10^{-5}	33.4
[5,6] cm	4.86×10^{-5}	41.2
[6,7] cm	2.77×10^{-5}	58.3
[7,8] cm	9.89×10^{-6}	74.5

From Table 4-3, it can be seen that there is a lower total dose around the Bragg peak ([7,8] cm) which is also primarily deposited locally. From this, it follows that the assumption of local dose deposition works better around the Bragg Peak, which is why the in house algorithm approximates the Bragg peak with great precision, as can be seen in Figure 2-2.

To quantify the degree of error between the 3D dose matrix of the scored secondary protons and the 3D dose matrix of the secondary protons, which were obtained directly from TOPAS using the setup discussed Section 3-0-1. The IDD(z) and IDD(y) were derived for all the depths, which were then compared to the IDD's obtained from the TOPAS simulations. The IDD's are shown Figure 4-11 and 4-12.

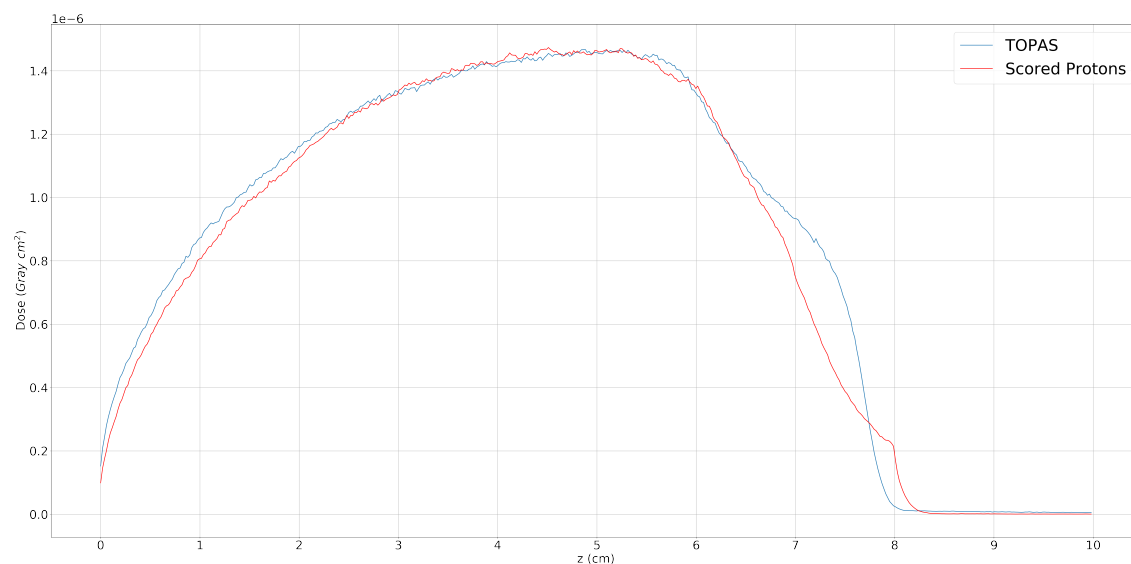


Figure 4-11: IDD(z) of the Scored secondary protons and the IDD(z) obtained through the simulation setup described in section 3.1

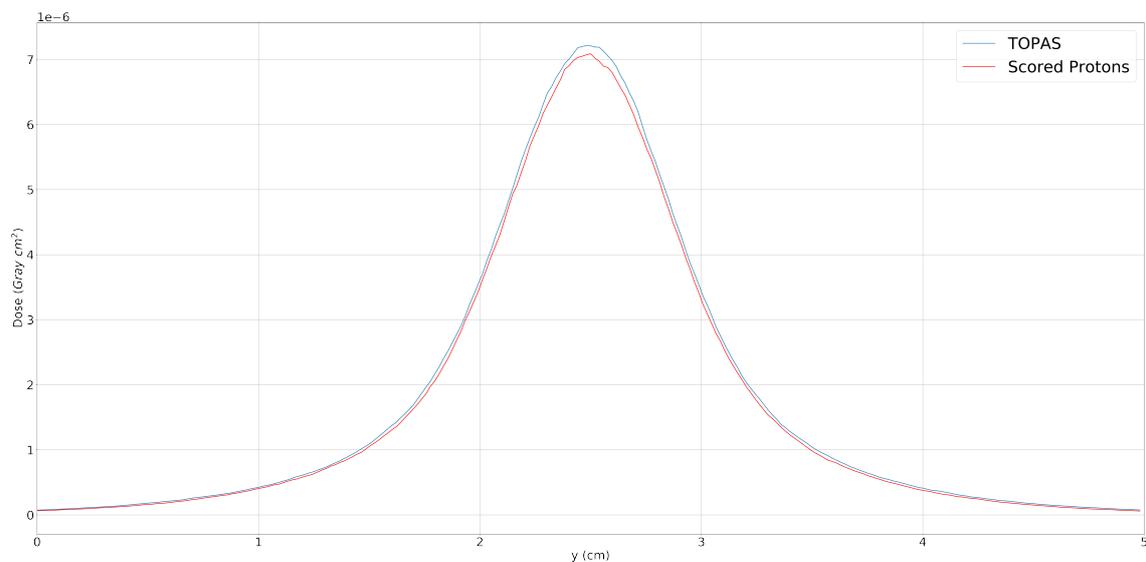


Figure 4-12: IDD(y) of the Scored secondary protons and the IDD(y) obtained through the simulation setup described in section 3.1

From Figure 4-11 and 4-12 it can be seen that the scored protons approximate the integrated depth doses in both y (and x) and z with great precision. For the IDD(z) the approximation breaks down around the Bragg Peak. This can be due the fact that the discrete measurement at the mean of the range can not be extrapolated to the entire range, due to the rapid decrease of dose in that range. The error in Figure 4-12 seems to be concentrated around the center beam which can largely be contributed to the absolute difference in dose between the 3D dose matrices from the scored protons and the 3D dose matrices obtained directly from TOPAS.

In order to further quantify the degree of error, the error is computed is computed by the following equation.

$$Error = \frac{1}{\sum_{i=1}^n T_i} \sum_{i=1}^n |S_i - T_i| \quad (4-3)$$

where S_i is equal to the IDD of the scored particles and T_i is equal to the IDD obtained through TOPAS. Using equation (4-3) the following degrees of error were obtained.

Table 4-4: IDD(z) and IDD(x/y) and the degree of error calculated using Equation 12.

IDD	Degree of error
IDD(z)	5.1%
IDD(x/y)	3.4%

The absolute difference between the sum of the 3D dose matrix of the TOPAS simulation and the 3D dose matrix of the scored secondary protons is equal to 1.54×10^{-5} [Gy]. Which is equal to 0.096% of the total dose and 2.75% of the dose contributed by all secondary particles.

Using these obtained statistics it can be reasoned that the error in the dose deposition is insignificant and should not alter dose calculations in treatment plans.

Conclusion and recommendations for further research

5-0-1 Conclusions

In this thesis, the dose contributions of secondary particles were mapped and quantified to improve the current in house algorithm, which deposits all dose from nuclear interactions locally. By analyzing the dose contribution of each secondary particle and their potential to deposit dose non locally, it was found that only secondary protons deposited significant dose non locally as secondary protons accounted for 88% of the dose contributed by secondary particles. And had sufficient range to contribute that dose non locally.

In section 3-0-2, the secondary protons were then scored at the point of creation at $\frac{(2i-1)}{2}$ cm for $i=1,2..10$ with a spatial resolution of ± 0.02 cm using Phase Space scorers. From these Phase Space scorers, the angle and energy distributions were obtained, which gave insight in the changes in energy and angle distributions of the secondary protons over depth.

By using the scored particles as a source and scaling them appropriately, as was described in section 3-0-3, the 3D dose matrices of the secondary protons were obtained for each 1 cm range in the Water Box. The analysis of these 3D dose distributions showed that in the range of $[0,1]$ cm, the local dose deposition only accounts for 21.6% of the total dose deposited by the secondary protons in that region. This percentage increases with depth to 74.5% at the $[7,8]$ cm range.

The findings show that the assumption made for the in house algorithm becomes more accurate with depth, which explains the accuracy in Figure 2-2 around the Bragg peak. In order to quantify the inaccuracy of the derived 3D dose distributions, the $IDD(z)$ and $IDD(x/y)$ of both the scored secondary protons and the IDD obtained through TOPAS were obtained. By calculating the relative error it was found that the $IDD(z)$ differs by 5.1% and that the $IDD(x/y)$ differs by 3.4%. The absolute difference is equal to 1.54×10^{-5} Gy, which accounts for 0.096% of the total dose and 2.75% of the dose deposited by all relevant secondary particles.

The obtained difference suggests that the methodology described in Chapter 3 can approximate the 3D dose matrix of the secondary protons to a large degree. The absolute error of 1.54×10^{-5} Gy combined with the relative biological effectiveness of protons indicate that the absolute error in dose should not significantly alter dose calculations for treatment planning. Thus the results suggest that in the geometry utilised in this thesis, the pre-calculated 3D dose matrix can improve the current in house algorithms accuracy.

The addition of the pre-calculated 3D dose matrix will result in a lower dose deposition at the entrance region and thus get closer to the theoretical result. The 3D dose matrices can also be convolved with kernels for other materials to obtain approximate 3D dose distributions of more complex geometries.

5-0-2 Recommendations for further research

In section 5-0-1, it was concluded that the methodology described in chapter 3 approximates the relevant secondary particles to a high degree. However, the methodology contains its limitations and approximations, which result in inaccuracies. In this section, these limitations and approximations will be discussed together with recommendations for further research to limit inaccuracies.

In section 3-0-2, the usage of a Phase Space scorer is introduced to score the energy and angle distributions of secondary particles created within a particular range. However, the Phase Space scorer has several flaws due to its ability to only score particles that reach its surfaces. This causes the scorer to omit particles with a low range, which is an even larger problem for particles with a significant angular deviation from the beam as these particles have to travel a relatively larger range. This can also cause bias towards particles with a small angular deviation from the beam path. In this thesis, this was a less relevant problem as particles which had a small average range were omitted. This inaccuracy is also limited by the reduction of the dimension in depth which reduces the required range. However this required more original histories as the probability of a secondary particle being created inside the Test Box, which is assigned a Phase Space scorer, decreases if the dimension in depth decreases. In further research, the spatial resolution can be further increased by creating Test Boxes with an even smaller depth dimension and increasing the number of original histories.

The position of the Test Boxes to which the Phase Space scorers and origin count filters are assigned in sections 3-0-2 and 3-0-3 also contribute to the inaccuracy. This is due to the assumption that the characteristics of the scored particles stay constant over the range of distribution (section 3-0-3). This is a reasonable approximation if the dose deposition stays relatively constant over depth but whenever this is not the case the assumption breaks down and causes inaccurate results as can be seen at $z=8$ cm in Figure 4-4. The same problem arises when scaling the dose using the origin count filter. In further research, this inaccuracy can be partially resolved by creating more Test Boxes which are assigned a Phase Space scorer/origin count filter, which reduces the range over which the assumption of constant distributions needs to hold, making the final 3D dose matrix more accurate. This will, however, increase the amount of data processing required.

Furthermore, the result can be improved by including all secondary particles to obtain the 3D dose distributions of all secondary particles instead of only the secondary protons. However, this would require alterations to the current methodology as Phase Space scorers are ineffective

for scoring particles with small ranges such as alpha particles. The addition of other secondary particles may not translate to a significantly better approximation of the total secondary dose as secondary protons already account for 88% of the secondary dose. However, omitting secondary particles such as alphas can cause the underestimation of the relative biological effectiveness as alpha particles have a significantly higher relative biological effectiveness than protons. Lastly, the 3D dose matrices of secondary particles can be derived using a varying primary proton beam energy to determine the relationship between primary proton energy and secondary proton dose distributions.

Chapter 6

Appendix

6-0-1 Configuration of DoseToMedium scorer

```
s:Sc/Doseall/Quantity = "DoseToMedium"  
s:Sc/Doseall/Component = "WaterTank"  
b:Sc/Doseall/OutputToConsole = "False"  
s:Sc/Doseall/IfOutputFileAlreadyExists = "Overwrite"  
sv:Sc/Doseall/Report = 1 "Sum"  
i:Sc/Doseall/XBins = 256  
i:Sc/Doseall/YBins = 256  
i:Sc/Doseall/ZBins = 512
```

DoseToMedium scorer which is assigned to the entire WaterTank as seen in the second line. The reported quantities are the sum of all dose in each voxel (Bin). This is the same configuration which is used when the source is equal to the scored secondary particles.

6-0-2 Configuration of Phase Space scorer

```
s:Sc/phsp1/OnlyIncludeParticlesOfGeneration = "Secondary"  
s:Sc/phsp1/Quantity = "PhaseSpace"  
s:Sc/phsp1/Surface = "TestBox1/AnySurface"  
s:Sc/phsp1/OutputType = "ASCII"  
s:Sc/phsp1/IfOutputFileAlreadyExists = "Overwrite"  
sv:Sc/phsp1/OnlyIncludeParticlesFromVolume = 1 "TestBox1"  
sv:Sc/phsp1/OnlyIncludeParticlesNamed = 6 "proton" "neutron" "deuteron" "triton" "alpha"  
"He3"
```

The Phase Space scorer which is assigned to a Test Box and is filtered to on only score the most probable secondary particles which are created within the Test Box.

6-0-3 Configuration of OriginCount scorer

```
s:Sc/ProtonOrigin/OnlyIncludeParticlesOfGeneration = "Secondary"  
s:Sc/ProtonOrigin/Quantity = "OriginCount"  
s:Sc/ProtonOrigin/Component = "TestBox1"  
sv:Sc/ProtonOrigin/OnlyIncludeParticlesNamed = 1 "proton"  
s:Sc/ProtonOrigin/IfOutputFileAlreadyExists = "Overwrite"
```

OriginCount scorer which is assigned to a Test Box and only counts the amount of secondary protons created within. The size of the Test Boxes were changed created as was stated in section 3-0-3.

Bibliography

- [1] Tian Xiufang, Kun Liu, Yong Hou, Jian Cheng, and Jiandong Zhang. The evolution of proton beam therapy: Current and future status (review). *Molecular and Clinical Oncology*, 11 2017.
- [2] Martin J. Berger. Penetration of Proton Beams Through Water I. Depth-dose Distribution, Spectra and LET Distribution. *NISTIR*, 1993.
- [3] National Institutes of Health. Cancer. <https://www.cancer.gov/about-cancer/understanding/what-is-cancer>, 2021. [Online; accessed 22-January-2022].
- [4] Michael Baumann, Mechthild Krause, Jens Overgaard, Jürgen Debus, Søren M. Bentzen, Juliane Daartz, Christian Richter, Daniel Zips and Thomas Bortfeld. Radiation oncology in the era of precision medicine. *Nature Reviews Cancer* 16(4):234, 2016.
- [5] Harald Paganetti. Range uncertainties in proton therapy and the role of monte carlo simulations. *NPhys Med Biol*. 2012 June 7; 57(11): R99–R117.
- [6] J.Kirana. The biological effects of breathing interplay in proton therapy treatments. TU Delft, 2021.
- [7] Harald Paganetti. Proton therapy physics. CRC press, 2018.
- [8] S.M. Seltzer,P.M. Bergstrom. Stopping-Power Range Tables for Electrons, Protons, and Helium Ions. <https://www.nist.gov/pml/stopping-power-range-tables-electrons-protons-and-helium-ions>, 2017. Online; accessed 29 January 2022.
- [9] Uilkema, S. B. Proton therapy planning using the sn method with the fokkerplanck approximation. TU Delft, 2012.
- [10] Stephen M. Seltzer. An assessment of the role of charged secondaries from nonelastic nuclear interactions by therapy proton beams in water. NTIS, U.S. Department of Commerce, Springfield, VA 22161.

-
- [11] Harald Paganetti. Nuclear interactions in proton therapy: dose and relative biological effect distributions originating from primary and secondary particles. *Physics in Medicine and Biology*, 47(5), 747–764.
- [12] T.Burlacu. Gauging the effect of energy straggling on proton dose distributions. *TU Delft*, 12 2019.
- [13] B. Faddegon, J. Ramos-Mendez, J. Schuemann, A. McNamara, J. Shin, J. Perl, and Paganetti H. The TOPAS Tool for Particle Simulation, a Monte Carlo Simulation Tool for Physics, Biology and Clinical Research. *Physica Medica*, 2020.
- [14] Duderstadt, J. J., Hamilton, L. J., Moorthy, S., Scott, C. C. . Nuclear reactor analysis. . *IEEE Transactions on Nuclear Science*, 24(4), 1983.
- [15] M.Romme. Approximating the effects of uncertainties in proton therapy using adjoint theory. *TU Delft*, 6 2020.
- [16] Mohammad Asadzadeh Tobias Gebäck. Analytical Solutions for the Pencil-Beam Equation with Energy Loss and Straggling. *Transport Theory and Statistical Physics*, 41:5-6, 325-336, 2012.
- [17] G. Folger, J.P. Wellisch. The binary cascade. <https://cds.cern.ch/record/865824/files/p313.pdf>, (visited on 12-02-2022).
- [18] Geant4 Collaboration. Geant4 Guide For Physics list Release 11.0. https://geant4.web.cern.ch/support/user_documentation (accessed on February 5, 2021).